Searching for the Higgs

Chris Tully

SSI 2006

version date: July 20, 2006

Contents

0.1. From LEP2 to the LHC

- *M. Kado and C. Tully, "The Searches for Higgs Bosons at LEP", ARNPS (2002) 52:65-113.*

An interesting comparison can be made between the experimental approach to the Higgs boson searches at LEP2 with those under preparation for the LHC. After early experimental measurements at the Z peak closed the door to the possibility of a Standard Model Higgs boson with a mass in the range $0 - 60$ GeV, a new era of direct searches for on-shell diboson(ZH) production began in 1996 when LEP increased the center-of-mass energy above ~ 160 GeV and continued through 2000 to the ultimate LEP energy reach of $\sqrt{s} = 209$ GeV. During this time, the event signatures were categorized according to the decay modes of the predicted Higgs boson and the well-studied decay modes of the Z boson, as shown in Figure 1. The Standard Model Higgs was searched for in its dominant decays into 3^{rd} generation fermions, i.e. tau leptons and bottom quark pairs.

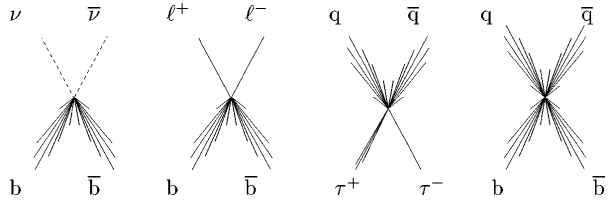

Figure 1: Topologies involved in the search for the standard-model Higgs boson at LEP2, missing energy, lepton pairs, $H \to \tau^+\tau^-$ and hadronic Z decays, four-jets.

Coverage was essentially complete ($\sim 90\%$) achieving a maximum detection efficiency with varying degrees of sensitivity to the observation of a Higgs boson above Standard Model background processes with similar experimental signatures. The closest "Higgs-like" backgrounds came from ZZ production with at least one Z boson decaying to $b\bar{b}$, noting the finite and non-Gaussian detector resolution on the measurement of the dijet $b\bar{b}$-mass. An example four-jet event is shown in Figure 2.

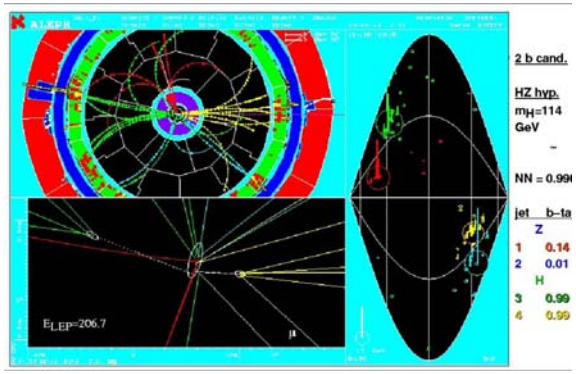

Figure 2: ALEPH four-jet event.

In the missing energy channel of the Higgs search, some contribution to the sensitivity came from WW fusion, a process whereby both the incoming positron and electron covert to neutrinos radiating W bosons which fuse to form the Higgs boson, as shown in Figure 3. This exceptional process becomes a larger fraction of the total Higgs production rate with increasing beam energy. An example missing energy event is shown in Figure 4.

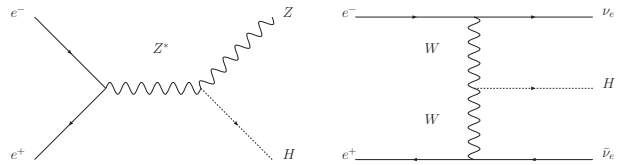

Figure 3: Diagrams of the Higgs-strahlung and weak boson fusion processes of Higgs boson production at LEP2.

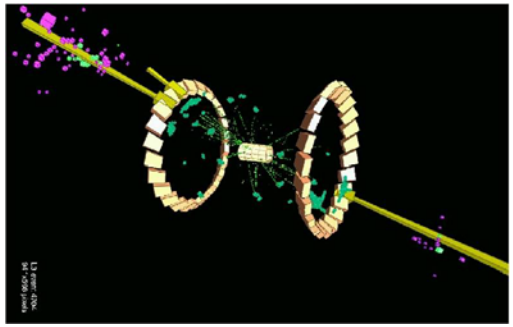

Figure 4: L3 missing energy event.

Many analysis techniques were used to quantify the agreement of the overall contributions of Standard Model processes to the Higgs search background predictions, and in all cases the level of agreement was exceptional with comparably small theoretical and experimental uncertainties, as shown in Figure 5. Therefore, background systematic uncertainties have little contribution to the overall search sensitivity. An important aspect of the LEP searches was the use of event-by-event discrimination that was sensitive to event counting as well as properties such as reconstructed mass. The final LEP measure of the Higgs search data quantified both mass and rate information, as shown in Figure 6, where the presence of a Higgs boson signal formed a minimum in the likelihood ratio.

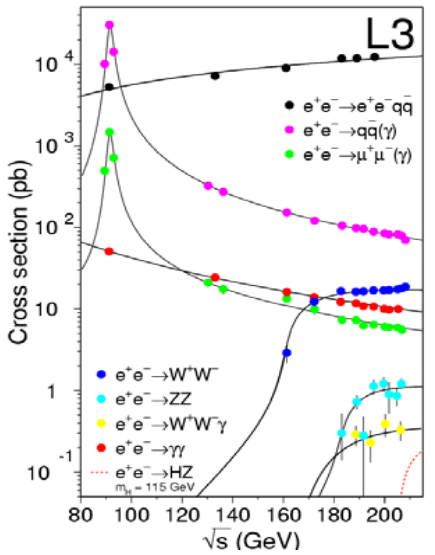

Figure 5: Cross section measurements by the L3 Experiment at LEP2.

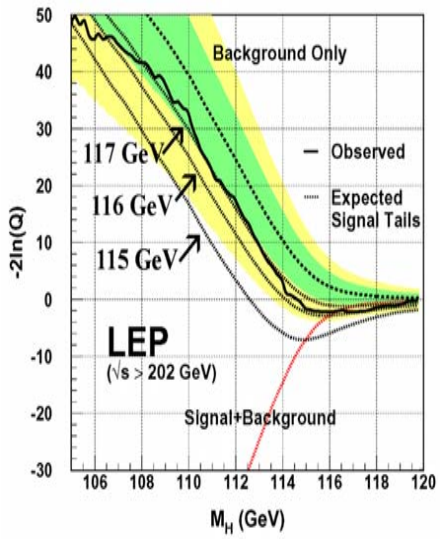

Figure 6: LEP-combined SM Higgs Search Data.

The ZH cross section turns on rapidly above threshold while at the same time, the magnitude of the cross section near threshold is comparatively small, as shown in Figure 5. With four LEP experiments, sensitivity to a 60 fb cross section at the kinematic limit of $m_H = \sqrt{s} - m_Z$ was achieved with ~ 200 pb^{-1} delivered per experiment. From an LHC point-of-view, what matters is the expected significance versus mass for a Standard Model Higgs for the LEP combined integrated luminosity, and this is shown in Figure 7.

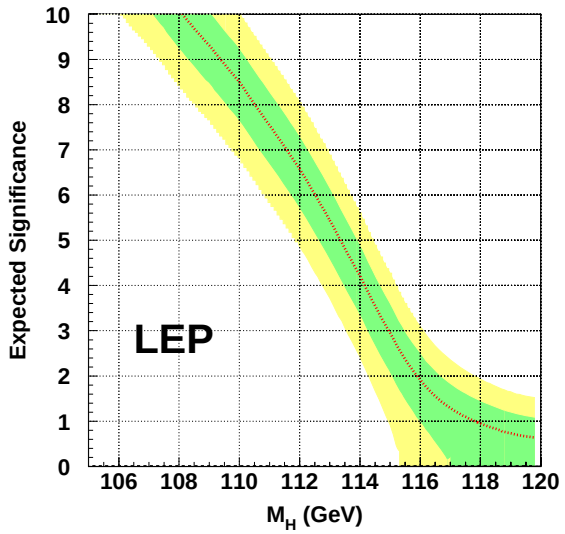

Figure 7: Expected significance for a Standard Model Higgs boson with the entire LEP2 dataset.

At the LHC, the LEP approach of searching in all available final state topologies is still a valuable starting point for the construction of the analyses. However, the high rate hadron collider backgrounds overwhelm fermionic Higgs decays into bottom quark pairs and even the low mass inclusive tau pair decays. Judicious choice of final state search topologies must also accommodate the triggering capabilities of the experiment. The trigger limitations impact final states with low $p_{\rm T}$ single leptons or jets. At the LHC, there are few cases of low background search channels, and more of the leverage comes from high resolution mass reconstruction or large multi-lepton rates. In particular, search channels that require counting a fixed number of jets to isolate a process, such as separating the Standard Model W boson pair production events from top pair production, are very inefficient due to combination of low jet reconstruction efficiency at low $p_{\rm T}$ and the abundance of low $p_{\rm T}$ jets from initial state gluon radiation, minbias pile-up and the underlying event. Search channels with multijet QCD backgrounds tend to be more inclusive in order to simultaneously fit the dominant Standard Model background fractions. Some backgrounds are necessarily estimated using data-based samples as opposed to Monte Carlo simulation. The possibility of concurrent signals such as from multiple Higgs bosons and the presence of SUSY particle production also warrant wider event sample scrutiny, not to mention the large experimental challenges of commissioning the detector in all

necessary aspects of the measurement.

The justification for the many experimental "warning flags" for LHC analyses is discussed in the following sections. The many possible manifestations of the Higgs boson discovery and crucial first measurements are also discussed.

0.2. Standard Model Higgs Search

The Standard Model Higgs production cross sections at the LHC and branching fractions are plotted in Figures 8 and 9, respectively.

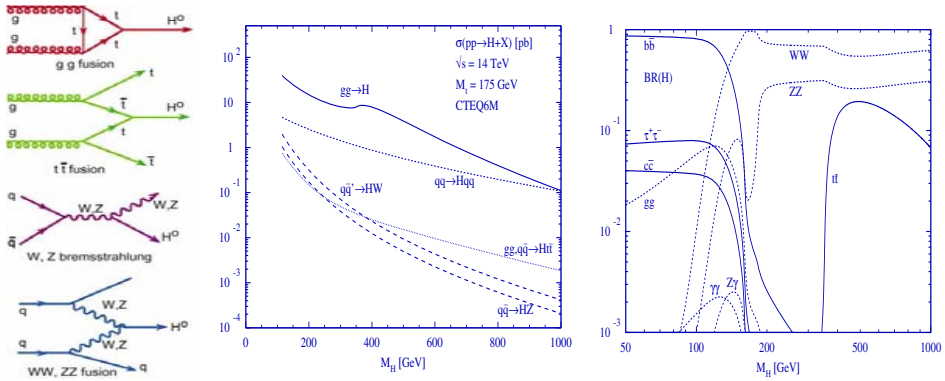

Figure 8: Standard Model Higgs Production Cross Sections.

Figure 9: Standard Model Higgs Decay Branching Fractions.

At low Higgs mass, $m_H \approx 115$ GeV/c^2, the dominant production process is gluon-gluon fusion with a cross section $\times 1000$ times larger than the corresponding LEP Higgs search. The WW fusion process is much stronger at the LHC due to the relatively low mass scale of the Higgs boson relative to the proton beam energy. The smallest relevant production rates are due to Higgsstrahlung processes from the heaviest known elementary particles WH, ZH and $t\bar{t}$H. The most dramatic aspect of the LHC Higgs searches is the transition in branching fractions from 3^{rd} generation fermion dominated decays to diboson dominated decays.

Folding the Higgs production cross sections and branching fractions (Figs. 8 and 9) against the trigger and selection efficiencies, a preliminary list of relevant search channels for a low mass Higgs search can be formed. This is given in Table 1. Of the channels in the left-most column, only the diboson decays of the Higgs are sufficiently clean to be detected inclusively within corresponding specific trigger paths. The columns to the right are a set of exclusive decay channels where identification of associated production particles give at least an order of magnitude improvement in signal to background separation, relative to the inclusive searches. The exclusive channels have unique sensitivities to 3^{rd} generation Higgs couplings, tree-level electroweak couplings and more precise mass and partial decay width measurements.

DECAY	Production	Inclusive (including gg fusion)	Weak boson fusion	WH/ZH	ttH
H→γγ		YES	YES	YES	YES
H→bb					YES
H→ττ			YES		
H→WW*		YES	YES	YES	
H→ZZ*, Z→ℓ⁺ℓ⁻, ℓ=e,μ		YES			
H→Zγ, Z→ℓ⁺ℓ⁻, ℓ=e,μ		very low			

Table 1: The most important SM Higgs channels for m_H below the WW-threshold.

In the 20 GeV mass range between the WW and ZZ-thresholds, the inclusive WW channel is the dominant decay mode with substantial statistics to form a transverse mass measurement of the Higgs. Above the ZZ-threshold, the four-lepton decay is the golden channel for Higgs discovery with low backgrounds and high resolution mass reconstruction in a mixture of pairs of dielectron and dimuon decays.

At the highest masses, the dropping production cross sections are compensated by the addition of hadronic W and Z decay modes. The high p_T boson signature has lower backgrounds and the dijets begin to merge, providing a clear massive monojet signature. Similarly, the neutrino decays of high p_T Z bosons provide a substan-

tial transverse missing energy. These highly boosted diboson decays provide Higgs boson search coverage up through 1 TeV/c^2 where the width of the Higgs becomes comparable to its mass and the electroweak scattering of massive weak bosons will begin to form resonances in a semi-strong coupling regime. Thus, 1 TeV/c^2 marks the upper limit to the production of a meaningful particle excitation of the Standard Model Higgs field.

0.2.1. High Mass Resolution Search Channels

The sub-threshold decay of the Higgs boson to ZZ* is kinematically similar to a semileptonic b-quark decay in that dominantly one Z boson is nearly on-shell and the second Z boson has a mass corresponding to the remaining Q^2 of the decay. Therefore, a 130 GeV/c^2 Higgs boson will decay into a ~ 90 GeV/c^2 and a less than 40 GeV/c^2 pair of Z bosons. The soft Z boson decay into leptons is problematic in terms of lepton backgrounds and reconstruction efficiency. Ultimately, low p_T lepton detection and diminishing ZZ^* branching fraction limit this channel to above 130 GeV/c^2.

Background to $H \rightarrow 4\ell$ comes from $t\bar{t}$ dilepton decays with both b-jets producing

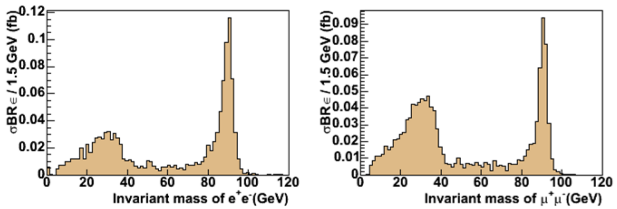

Figure 10: Dilepton mass distributions for $H \rightarrow ZZ^* \rightarrow 2e2\mu$, $m_H = 130$ GeV/c^2, on the left for dielectrons and on the right for dimuons. The low mass dimuons are enhanced because of the high muon reconstruction efficiency at low p_T.

leptons from semi-leptonic decays. Similarly, the process $Zb\bar{b}$ is also a background with a Z decaying to leptons and each b-jet producing a lepton (for background studies replace "b" everywhere with lepton). Note, leptons from B-hadron semileptonic decay can be partially removed using impact parameter techniques (4ℓ vertex probability) as well as lepton isolation.

The above-threshold $H \rightarrow ZZ$ decay has irreducible background from on-shell ZZ production, as shown in Figure 11.

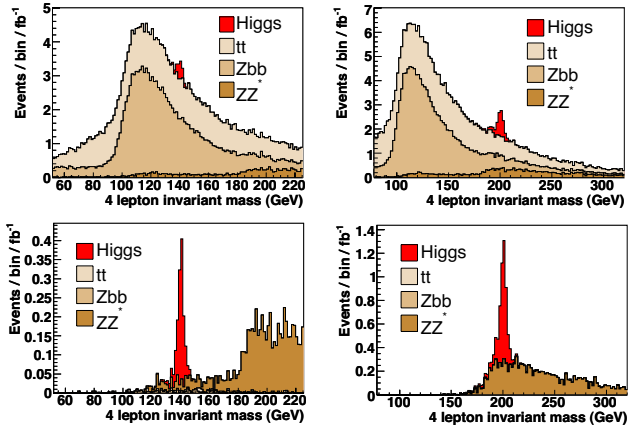

Figure 11: The $H \rightarrow ZZ^* \rightarrow 2e2\mu$ mass distributions before (top) and after (bottom) final selections for $m_H = 140$ GeV/c^2 (left) and $m_H = 200$ GeV/c^2 (right).

The number of selected signal and background varies strongly with mass as shown in Figure 12 with a corresponding signal significance shown in Figure 13. With

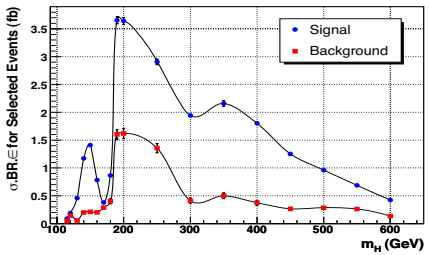

Figure 12: Cross section after acceptance $H \rightarrow 2e2\mu$.

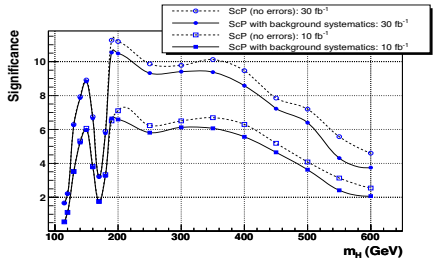

Figure 13: Signal significance for $H \rightarrow 2e2\mu$.

a mass resolution of $1.0 - 1.2\%$, the direct measurement of the width Γ_H becomes possible above $\sim$ 200 GeV/c^2 as shown in Figure 14. Note, the growth of the Higgs width beyond 30-40 GeV/c^2 is a feature of the Standard Model Higgs boson. An anomalously narrow high mass Higgs would indicate a preference for fermionic

decay modes, as predicted in many regions of the MSSM Higgs sector.

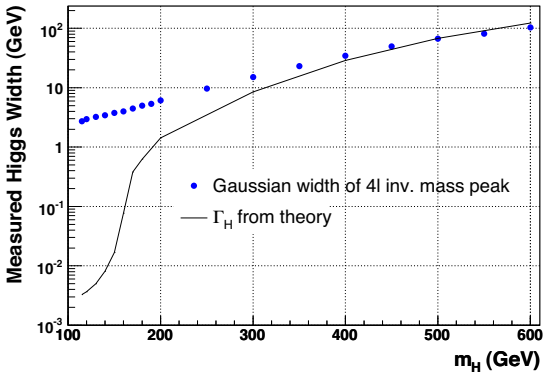

Figure 14: Direct measurement of the Higgs width becomes possible above $\sim$ 200 GeV/c^2 in the $H \rightarrow 2e2\mu$ channel.

In addition to being a dominant discovery mode, the $H \to ZZ \to 4\ell$ decay mode is a powerful probe of the spin, parity and CP. The most general HZZ vertex factor can be written in terms of the four-momenta of the Z bosons, k_1 and k_2, and the four-momentum of the Higgs boson, $p \equiv k_1 + k_2$, and is given by

$$\frac{igM_Z}{\cos\theta_W}\left(ag_{\mu\nu} + b\frac{p_\mu p_\nu}{M_Z^2} + c\epsilon_{\mu\nu\rho\sigma}\frac{k_1^\rho k_2^\sigma}{M_Z^2}\right) \quad (1)$$

where the first term corresponds to the SM scalar, the second to a non-SM scalar and the third to a non-SM pseudoscalar. CP-violation would be present for admixtures of non-zero a, b and c in equation (1). The experimental observables are the azimuthal and polar angular distributions. The azimuthal angle ϕ is measured between the two planes defined by the leptonic decays of the two Z bosons in the Higgs rest frame, as shown in Figure 15. This yields a distribution

$$F(\phi) = 1 + \alpha\cos\phi + \beta\cos 2\phi \ . \quad (2)$$

The polar angle is defined in the rest frame of each of the Z bosons and is the the angle between the negatively charged lepton and the direction of motion of the Z boson in the Higgs boson rest frame, as shown in Figure 15. The polar angle distribution has the form

$$G(\theta_{1,2}) = T(1 + \cos^2\theta_{1,2}) + L\sin^2\theta_{1,2} \ . \quad (3)$$

One defines the asymmetry $R = \frac{L-T}{L+T}$ to better distinguish the models. The helicity

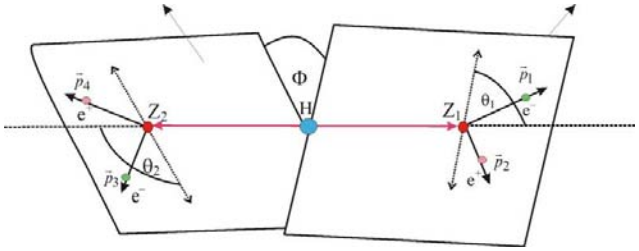

Figure 15: Definition of decay angles in Higgs reset frame.

amplitude of the $|ZZ\rangle$ state to be in the $|00\rangle$ state is predicted to be

$$T_{00} = \frac{M_H^2 - 2M_Z^2}{2M_Z^2} \text{ for } M_H > 2M_Z \ . \quad (4)$$

The value of R for a $S^{CP} = 0^+$ state is $R = \frac{T_{00}^2-1}{T_{00}^2+1}$ and for a $S^{CP} = 0^-$ state, $R = -1$. The predicted values of R for SM Higgs production are given in Figure 16.

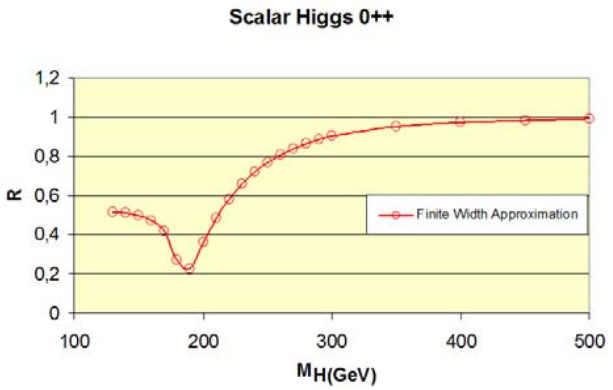

Figure 16: Standard Model prediction for R.

The highest resolution of the high resolution Higgs search channels is the $H \to \gamma\gamma$ decay. If the high energy photons from the Higgs decay propagate through the beam pipe and tracker volume without conversion and are stopped by a high resolution electromagnetic calorimeter, then an event-by-event mass measurement resolution below 1 GeV/c^2 can be achieved. The $H \to \gamma\gamma$ search is relevant for masses between 110-140 GeV/c^2 and is typically the single most sensitive low mass search channel. An event display is shown in Figure 17, with Figure 18 showing the current state of the physical CMS detector assembly.

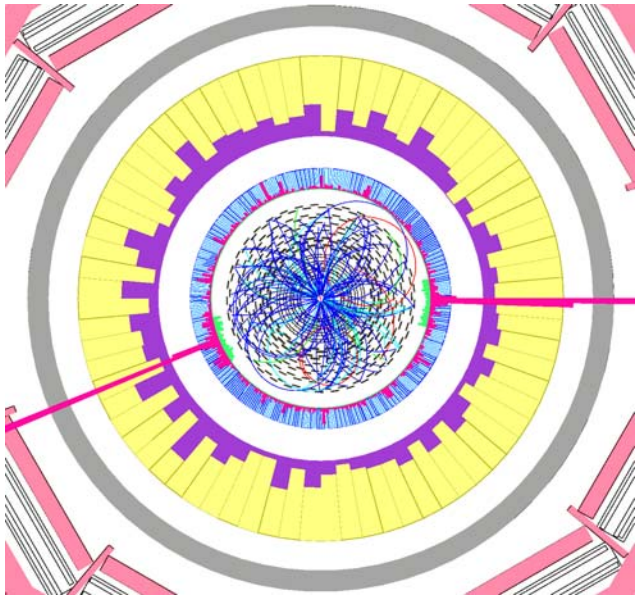

Figure 17: Simulation of a $H \rightarrow \gamma\gamma$ event in the CMS detector.

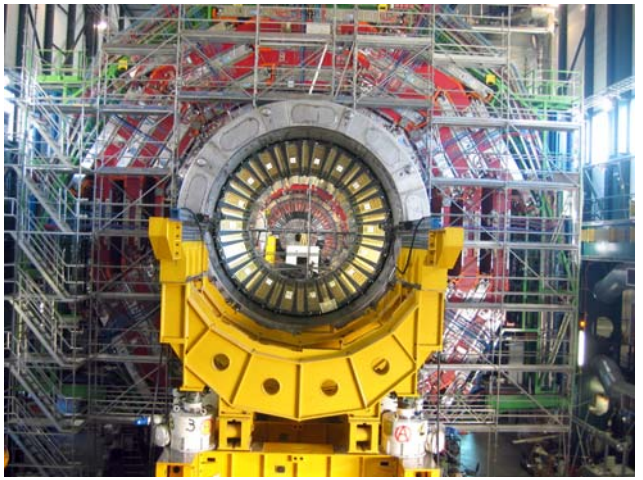

Figure 18: Current state of the CMS detector assembly.

The $H \rightarrow \gamma\gamma$ branching fraction is naturally expected to rise and then drop off on approaching the WW-threshold. This can be seen from the loop-diagrams of Figure 19 which have $Q^2 \approx 4M_W^2$. The negative interference between the top

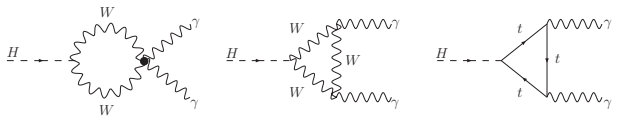

Figure 19: Loop diagrams for $H \rightarrow \gamma\gamma$ decay.

(fermion) and W boson loops decreases the partial decay width by $\sim 10\%$.

The contributions to the total Higgs production cross section at $m_H = 120$ GeV/c^2 are given in Table 2. The irreducible backgrounds, i.e. those with two real photons in the final state, come from:

- $gg \rightarrow 2\gamma$ (Box diagram)
- $q\bar{q} \rightarrow 2\gamma$ (Born diagram)
- $pp \rightarrow 2\gamma + jets$ with two prompt photons

while the reducible backgrounds come from neutral jets (or hard π^0's) that fake one

M_H	115 GeV/c^2	120 GeV/c^2	130 GeV/c^2	140 GeV/c^2	150 GeV/c^2
σ (gg fusion)	39.2 pb	36.4 pb	31.6 pb	27.7 pb	24.5
σ (WVB fusion)	4.7 pb	4.5 pb	4.1 pb	3.8 pb	3.6
σ (WH, ZH, $t\bar{t}$H)	3.8 pb	3.3 pb	2.6 pb	2.1 pb	1.7
Total σ	47.6 pb	44.2 pb	38.3 pb	33.6 pb	29.7
H $\rightarrow \gamma\gamma$ Branching Ratio	0.00208	0.00220	0.00224	0.00195	0.00140
Inclusive $\sigma \times B.R.$	99.3 fb	97.5 fb	86.0 fb	65.5 fb	41.5 fb

Table 2: Cross section and branching fraction for $H \rightarrow \gamma\gamma$, $m_H = 120$ GeV/c^2.

or two photons in the processes $pp \rightarrow \gamma + jet$ and $pp \rightarrow jets$, respectively. The process of two neutral jets faking a pair of high energy photons cannot be reliably simulated with Monte Carlo techniques. Data-driven techniques will be needed to estimate these backgrounds through the process of tightening photon isolation variables using sideband regions of the reconstructed Higgs mass, as in Figure 20.

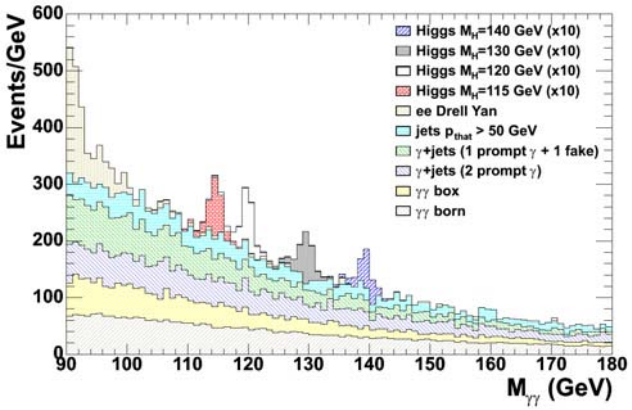

Figure 20: Reconstruction mass distribution for $H \rightarrow \gamma\gamma$ scale up by $\times 10$ on top of simulated background predictions. The statistics on the background predictions are limited.

The overall selection efficiency for Higgs decays to photons at $m_H = 120$ GeV/c^2 is $\sim$ 32% with contributions listed in Table 3. The corresponding backgrounds for this selection are given in Table 4 with large uncertainties in the $pp \rightarrow jets$ contribution. For 1 fb^{-1} of integrated luminosity and a 2.5 GeV mass window, the expected number of $H \rightarrow \gamma\gamma$ events is 27 for a background of 445 events, giving an $S/B \sim 6\%$. For comparison, at LEP, cutting out search regions with $S/B < 5\%$ had little effect on the search sensitivity, indicating a stark contrast with the LHC Higgs search.

After photon selection	+ tracker isolation	+ calorimeter isolation	accepted cross section	± 1 GeV mass window
50%	35%	32%	31 fb	17.6 fb

Table 3: Higgs selection efficiency and accepted cross section for $H \rightarrow \gamma\gamma$, $m_H = 120$ GeV/c^2.

The predicted $H \rightarrow \gamma\gamma$ search sensitivity depends strongly on the calorimeter resolution, as shown in Figures 21 and 22. Part of the resolution contribution is from primary vertex assignment which correctly assigns the signal vertex in $\sim$ 81% of the events at low luminosity. The current technique consists of assigning the ver-

Process	115 GeV/c^2	120 GeV/c^2	130 GeV/c^2	140 GeV/c^2
pp $\rightarrow \gamma\gamma$ (born)	48	44	36	29
pp $\rightarrow \gamma\gamma$ (box)	36	31	23	16
pp $\rightarrow \gamma +$ jet (2 prompt)	43	40	32	26
pp $\rightarrow \gamma +$ jet (prompt+fake)	40	34	22	19
pp $\rightarrow$ jets	29	27	20	18
Drell-Yan ee	2	2	1	1
Total background	203	178	134	109

Table 4: Estimated background expectations per unit of mass window (fb/GeV) for the $H \rightarrow \gamma\gamma$ inclusive search. A typical mass window is 2.5 GeV.

tex with the highest p_T track in the event as the $H \rightarrow \gamma\gamma$ signal vertex. Without an event-by-event vertex assignment, the invariant mass of the two-photon state is smeared by additional 1.5 GeV/c^2.

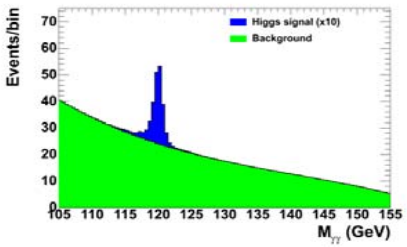

Figure 21: Comparison of signal and background distributions in $H \rightarrow 2\gamma$ for a calorimeter mass resolution of $\sigma_{m_H} = 700$ MeV at $m_H = 120$ GeV.

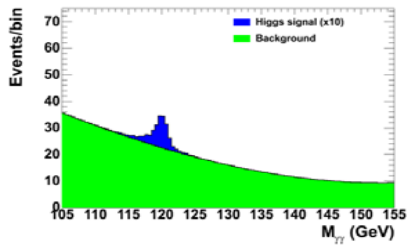

Figure 22: Comparison of signal and background distributions in $H \rightarrow 2\gamma$ for a calorimeter mass resolution of $\sigma_{m_H} = 900$ MeV at $m_H = 120$ GeV.

The gluon-gluon fusion loop-diagram for Higgs production is necessarily a high Q^2 process due to the top quark mass. It was proposed in Reference [S.Abdullin *et al.*, PLB 431: 410-419, 1998] that the search for $pp \rightarrow H \rightarrow \gamma\gamma + jet$ should have a higher signal-to-background ratio than the inclusive search by enhancing the contributions shown in Figure 23. The backgrounds are suppressed with a cut on $\sqrt{\hat{s}} > 300$ GeV, as in Figure 24. This channel also benefits from a more efficient primary vertex-jet assignment, using the tracks of the high p_T jet to assign the signal vertex.

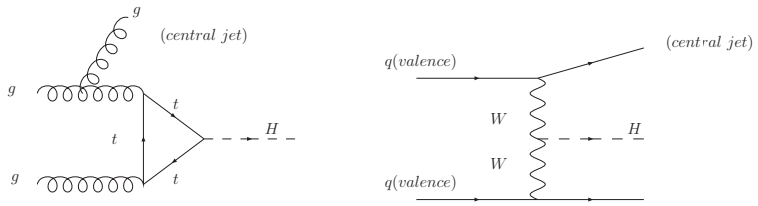

Figure 23: Two leading diagrams for $H \rightarrow 2\gamma + jet$ production. The diagram on the right is qqH weak boson fusion production of the Higgs boson.

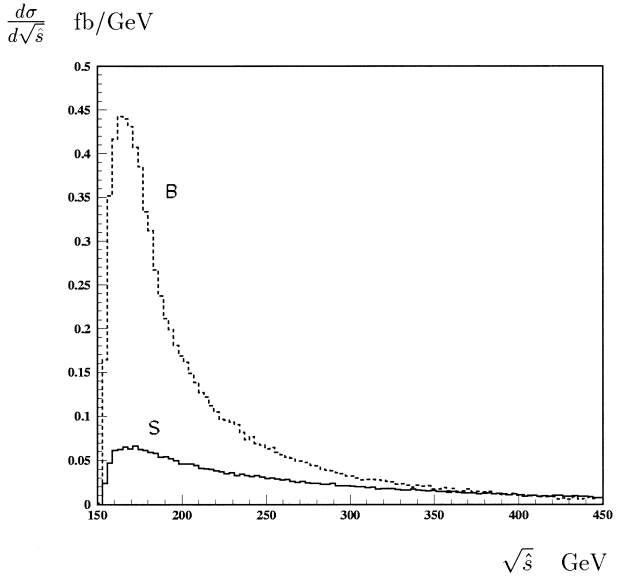

Figure 24: Distribution of the differential cross section in $\sqrt{\hat{s}}$ for the $H \rightarrow 2\gamma + jet$ signal(S) and background(B) processes.

The reduced background-level in $H \rightarrow 2\gamma + jet$ and in the weak boson fusion Higgs production will provide a flatter background shape on which to measure the mass of a light Higgs boson, as shown in Figures 25 and 26.

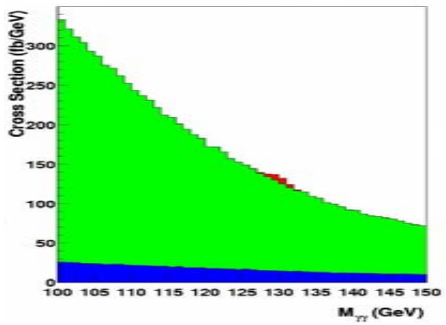

Figure 25: Comparison of signal and background distributions in the inclusive $H \rightarrow 2\gamma$ search, $m_H = 130$ GeV.

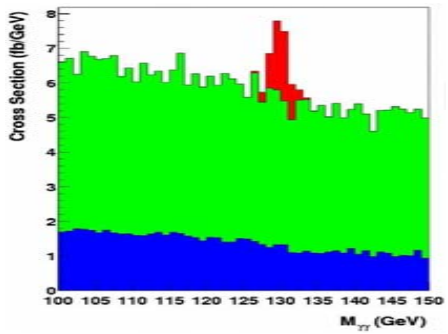

Figure 26: Comparison of signal and background distributions in $H \rightarrow 2\gamma + jet$, $m_H = 130$ GeV.

0.2.2. JetMET-Oriented Low-Mass Channels

There are three exclusive channels in the low mass Higgs search that compete with the $H \rightarrow \gamma\gamma$ sensitivity. These are $t\bar{t}H$ ($H \rightarrow b\bar{b}$), qqH ($H \rightarrow \tau\tau$) and qqH ($H \rightarrow WW^* \rightarrow 2\ell 2\nu$), as shown in Figure 27. All of these channels involve jets and transverse missing energy in the final state, and are therefore "JetMET"-related analyses. The resolution of jet p_T measurements are roughly an order of magnitude lower (worse) than corresponding electron, muon or photon measurements, as shown in Figure 29. The lower measurement resolution reduces the reconstruction efficiency of low p_T jets and introduces fake jets formed from low energy background sources. Thus, defining a search for final states involving a fixed number of low p_T jets has large inefficiencies and uncertainties.

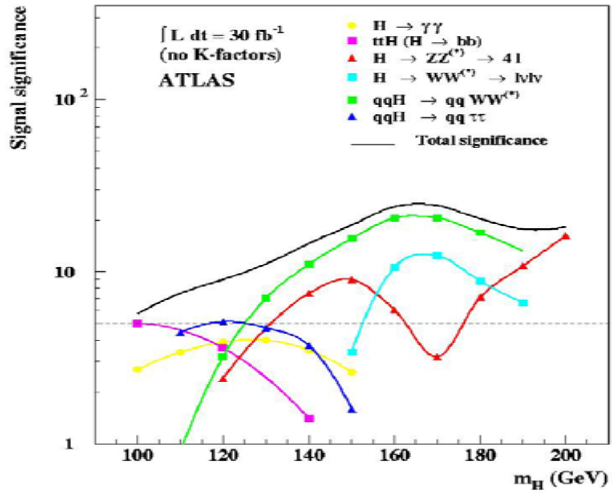

Figure 27: ATLAS Higgs search sensitivity in the low mass region.

The cross section for $t\bar{t}$ production at the LHC is ~ 840 pb, i.e. over a factor $\times 100$ larger than at the Tevatron, and therefore an abundant source of events. Figure 28 shows a mock commissioning plot from 150 pb^{-1} of simulated data. The cross section for associated Higgs production $t\bar{t}H$ is ~ 0.7 pb, three orders of magnitude smaller. While the 8-fermion final state of $t\bar{t}H$ with $H \rightarrow b\bar{b}$ appears to exceptionally rare to make the search channel unique, especially from the heavy flavor content, this is not the case in practice. The $t\bar{t}H$ search channel suffers from several sources of efficiency loss from branching fractions for $t\bar{t} \rightarrow \ell + jets$ and $H \rightarrow b\bar{b}$ (total branching fraction $\sim 20\%$), single-lepton trigger inefficiency, event selection when requiring exactly six jets, jet reconstruction efficiency, combinatorics of b-jet assignment, dijet $b\bar{b}$ mass resolution for defining a mass window and b-tagging efficiency to the fourth power, $\epsilon_b^4 \approx 11\%$. Figure 30 shows the reconstruction turn-on efficiency for jet reconstruction at an instantaneous luminosity of $\mathcal{L} = 2 \times 10^{33}\ cm^{-2}s^{-1}$ in the CMS calorimeter indicating low reconstruction efficiency for 10-15 GeV jets. At parton-level, the efficiency for the $t\bar{t}H$ channel decreases from 89%, 60%, 30% to 11% for corresponding p_T cuts on all partons of 10, 20, 30 and 40 GeV. Therefore, the use of tracking to enhance the calorimeter jet reconstruction and other techniques to sharpen the jet reconstruction efficiencies are essential to maintain low thresholds.

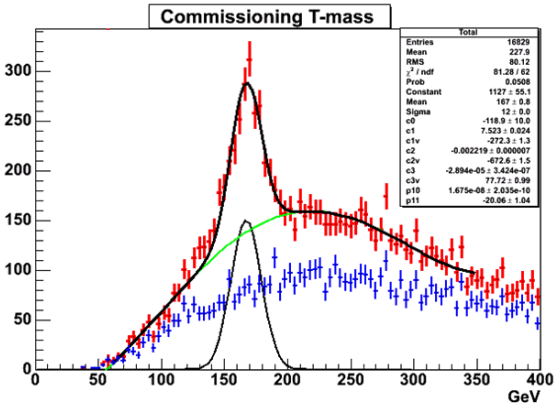

Figure 28: The three-jet hadronic top mass expected from calorimeter commissioning with 150 pb^{-1} of simulated data.

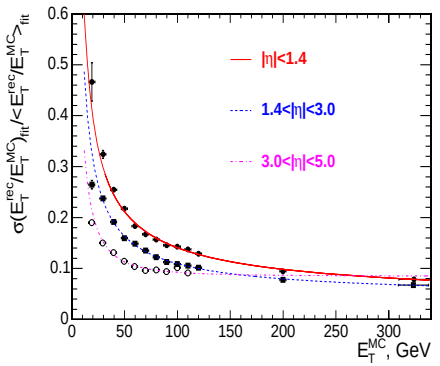

Figure 29: Calorimeter jet resolutions.

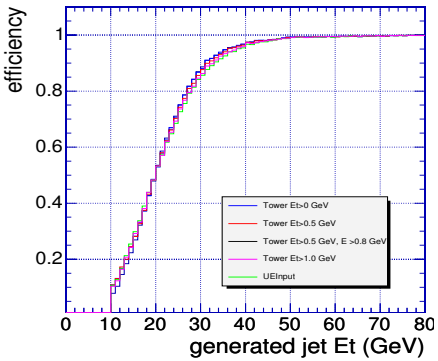

Figure 30: Turn-on curve of jet reconstruction efficiency for calorimeter jets in CMS.

An example distribution of the reconstructed Higgs mass in the $H \to b\bar{b}$ decay mode in $t\bar{t}H$ events is shown in Figure 31. The background shoulder is partially due to the $t\bar{t}Z$ background with $Z \to b\bar{b}$. The $b\bar{b}$ dijet mass resolution is expect to be $\sim 12 - 15\%$ and therefore separating m_Z and m_H will be limited by detector resolutions and calibrations. There is a broad contribution to the mass distribution from $t\bar{t}b\bar{b}$ production from QCD interactions, having more theoretical uncertainties in the shape and cross section than the $t\bar{t}Z$ process.

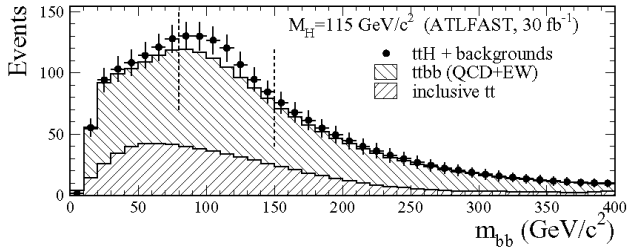

Figure 31: Higgs mass reconstruction in the $t\bar{t}H$ search.

Another JetMET-related channel is the weak boson fusion production qqH of the Higgs boson with the $H \to \tau\tau$ decay. In the decay of the Higgs to τ-leptons, a mass reconstruction technique involving the transverse missing energy aides in the separation of the large background from $Z \to \tau\tau + jets$. Only $\sim 80\%$ of the tau energy is visible in the calorimeter, the remainder is lost to neutrinos. Figure 32 shows how the transverse missing energy can be projected onto the τ-lepton momentum directions to recover part of the undetected tau energy. An example $H \to \tau\tau$ mass resolution for $m_H = 135$ GeV is shown in Figure 33.

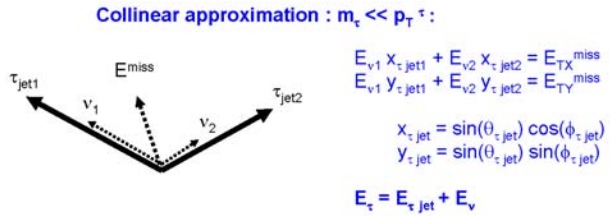

Figure 32: Mass reconstruction technique for $H \to \tau\tau$.

The effectiveness of using the measured $E_{\mathrm{T}}^{\mathrm{miss}}$ depends on the $E_{\mathrm{T}}^{\mathrm{miss}}$ resolution and

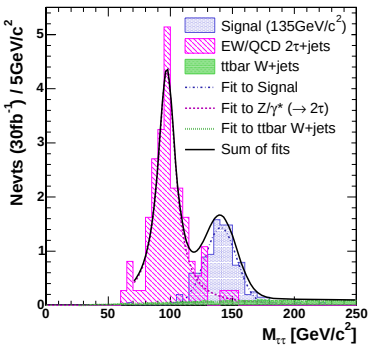

Figure 33: Reconstructed $\tau\tau$-mass using the $E_{\mathrm{T}}^{\mathrm{miss}}$ projection technique in the $H \to \tau\tau$ channel, $m_H = 135$ GeV/c^2.

resolution tails. Generally, the technique in Figure 32 requires a large Higgs p_T in order to avoid false solutions, typically only 40% of $H \to \tau\tau$ events have physical solutions using the $E_{\mathrm{T}}^{\mathrm{miss}}$ projection technique. An example of $E_{\mathrm{T}}^{\mathrm{miss}}$ resolution tails is given in Figure 34 for QCD dijet events, and a similar plot for the resolution as a function of the scalar $\sum E_T$ in Figure 35.

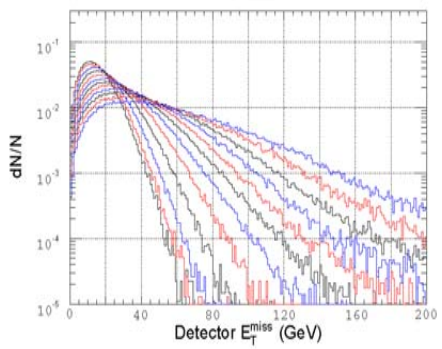

Figure 34: Transverse missing energy resolution tails in dijet events.

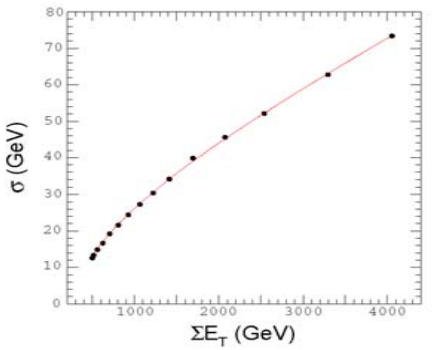

Figure 35: Transverse missing energy resolution in dijet events as a function of the scalar $\sum E_T$.

The effect of resolution tails is to throw intrinsically balanced background events into the event selection. The instrinsic Gaussian resolution of the missing transverse energy, on the other hand, is the primary parameter separating low mass Higgs events from the large $Z \rightarrow \tau\tau$ background, as seen in Figure 33. For events with no intrinsic $E_{\mathrm{T}}^{\mathrm{miss}}$, the direction of the measured $E_{\mathrm{T}}^{\mathrm{miss}}$ is correlated to the jet and lepton directions, as the mismeasurement of energetic objects is a leading source of p_T imbalance. The construction of an $E_{\mathrm{T}}^{\mathrm{miss}}$ significance, or a simple requirement on the minimum angular separation of the missing energy direction and the nearest jet or lepton, can substantially reduce backgrounds from high-rate intrinsically low $E_{\mathrm{T}}^{\mathrm{miss}}$ processes.

The selection efficiency for a pair of τ-leptons, such as from $H \rightarrow \tau\tau$ decay, has a substantial contribution from hadronic τ decays, as shown in Table 5. The

τ-pair final states	Branching fractions
$\tau_e\tau_{\mathrm{had}}$	22%
$\tau_\mu\tau_{\mathrm{had}}$	22%
$\tau_{\mathrm{had}}\tau_{\mathrm{had}}$	41%
$\tau_e\tau_\mu$	6%
$\tau_e\tau_e$	3%
$\tau_\mu\tau_\mu$	3%

Table 5: Tau pair final states involving electron(e), muon(μ) and hadronic(had) τ-lepton decays.

identification of hadronic tau decays relies on the narrowness and isolation of the tau jet. Figures 36 and 37 show the definition and performance, respectively, of a "shrinking cone" method for separating tau jets from QCD jets. Due to the finite mass of the tau, a higher p_T boost will result in a narrower jet of particles from its decay. The dominant 1-prong and 3-prong decays of the tau and the expected visible

mass distribution can be seen selected tau candidates, as shown in Figures 38 and 39 with Tevatron data.

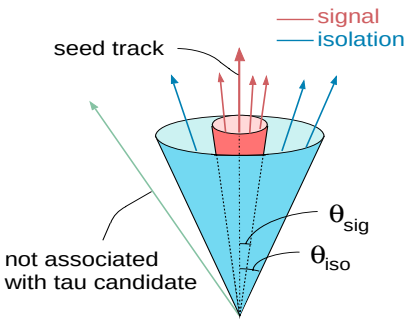

Figure 36: Tau Cone Definitions.

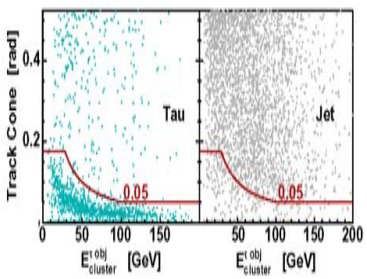

Figure 37: Jet/Tau Separation.

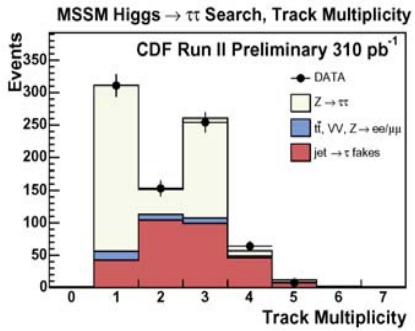

Figure 38: Track multiplicity in selected τ-lepton candidates before requiring an oppositely charged pair of τ-leptons in the event.

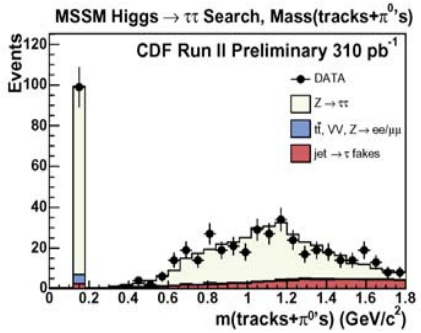

Figure 39: Reconstructed visible mass of selected τ-lepton candidates. The spike at the pion mass corresponds to 1-prong pion decays.

The triggering of qqH with $H \rightarrow \tau\tau$ relies on good hardware tau isolation techniques. Nominally, the signal signature is a four-jet final state with low $E_{\mathrm{T}}^{\mathrm{miss}}$ and therefore has a potentially overwhelming multijet QCD background. However, the kinematics of the forward-jets and the narrowness of the tau jets suppresses the multijet background. The pseudo-rapidity distributions of the jets and taus are plotted in Figure 40.

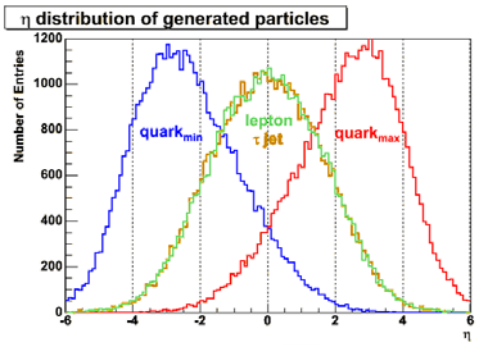

Figure 40: Forward-jet and τ-lepton pseudo-rapidity distributions in the qqH process with $H \rightarrow \tau\tau$.

An important background for the qqH search in the decay $H \rightarrow \tau\tau$ are $t\bar{t}$ events in the dilepton decay mode. The jets coming from this process are more central than forward-tagging jets from weak boson fusion and can be b-tagged if they are within the tracker acceptance, i.e. $|\eta| < 2.4$ for the CMS detector. Forward-tagging jets are light quark jets as they originate from valence quark scattering, see Figure 23. Therefore, the use of a central jet veto can be very powerful in reducing $t\bar{t}$ backgrounds. However, with ~ 5 multiple interactions at an instantaneous luminosity of $\mathcal{L} = 2 \times 10^{33} cm^{-2} s^{-1}$ (including single and doubly diffractive events), there are a number of minbias jets in every event with a p_T spectrum extending above 30 GeV. To maintain an effective central jet veto, the jets must be assigned to a vertex using the tracking information. The tracks of the central τ-jets define the primary vertex, and therefore the jets from the non-signal vertices are ignored in the central jet veto. Jet-vertex assignment will be important for all LHC measurements to reduce the effects of pile-up.

0.2.3. Inclusive Dilepton Analysis

The $H \rightarrow WW$ decay mode has a branching fraction of $\sim 8\%$ at $m_H = 115$ GeV/c^2 that grows steadily to a maximum of 96% right below the ZZ-threshold. The selection of WW events is only possible in the dilepton decay modes – the light quark jets from W decay are overwhelmed by low p_{T} jet background. Dilepton production is sufficiently suppressed at a hadron collider that the trigger system is able to maintain a high efficiency for all processes involving dileptons, with the exception high rates at low lepton $p_{\mathrm{T}} < 5$ GeV/c coming from inclusive J/Ψ production and B-hadron decay. The number of muons from hadron decay can be controlled to some degree by isolation requirements in the tracker and calorimeter. The additional requirement of prompt leptons, i.e. no significant displacement from the primary vertex, can be used to significantly suppress leptons from B-hadron decay. Table 6 gives a list of Standard Model processes contributing to the dilepton channel.

Dilepton Channel	$\sigma \times Br(\rightarrow 2\ell)\,(pb)$
Z/γ^*	145000
$t\bar{t}$	840
$b\bar{b} \rightarrow 2\mu$	710
$qq(gg) \rightarrow WW \rightarrow 2\ell$	11.7(0.54)
$Wt \rightarrow 2\ell$	3.4
$ZW \rightarrow 3\ell$	1.6
$ZZ \rightarrow 2\ell$	1.5

Table 6: Standard Model processes contributing to inclusive dilepton production and the corresponding cross section times branching ratio to dileptons.

The leptons from Higgs$\rightarrow WW$ tend to point in the same direction, as shown in Figure 41. This provides a natural search variable, namely $\Delta\phi_{\ell\ell}$ the azimuthal angle between the leptons. The high opening angle backgrounds come from $Z \rightarrow \tau\tau$ where both τ-leptons decay leptonically, as shown in Figure 42. The backgrounds in the reconstructed dilepton mass $m_{\ell\ell}$, shown in Figure 43 and 44 from the Tevatron, depend on the flavor combination of the leptons, where the $e\mu$ channel has substantially lower backgrounds from Drell-Yan and $Z \rightarrow \ell\ell$.

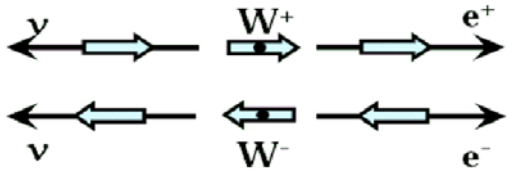

Figure 41: Leptons from $H \rightarrow WW$ decay tend to point in the same direction.

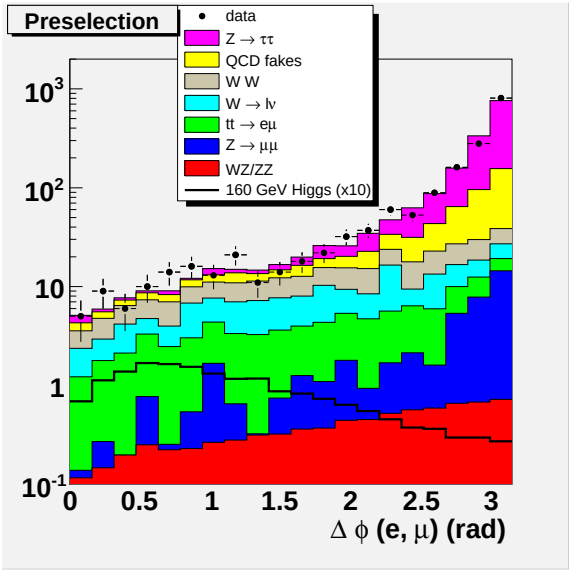

Figure 42: The azimuthal opening angle between leptons in the $H \rightarrow WW$ channel at the Tevatron.

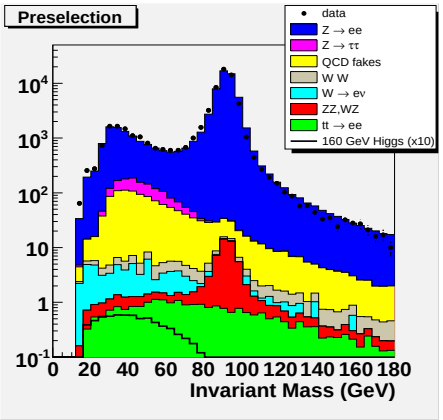

Figure 43: Reconstructed dilepton mass in $H \rightarrow WW \rightarrow ee$ channel.

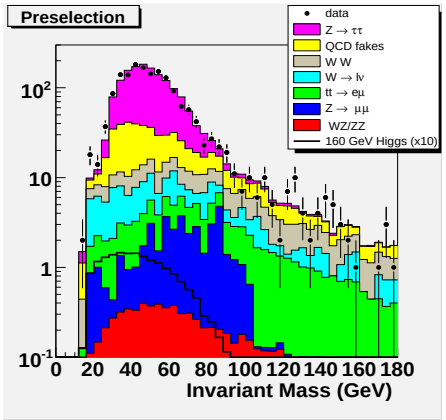

Figure 44: Reconstructed dilepton mass in $H \rightarrow WW \rightarrow e\mu$ channel.

The $t\bar{t}$, WW and $Z \rightarrow \tau\tau$ backgrounds to the $H \rightarrow WW$ search have differing dilepton kinematics, jet multiplicities and missing energy distributions. As it will be particularly difficult to fully separate samples with differing jet multiplicities and missing energy distributions, it is likely that a simultaneous "inclusive" dilepton analysis will be applied. An example analysis from the Tevatron is shown in Figure 46. In addition, the LHC will have new backgrounds such as flavor excitation production of $gb \rightarrow tW$, as shown in Figure 45.

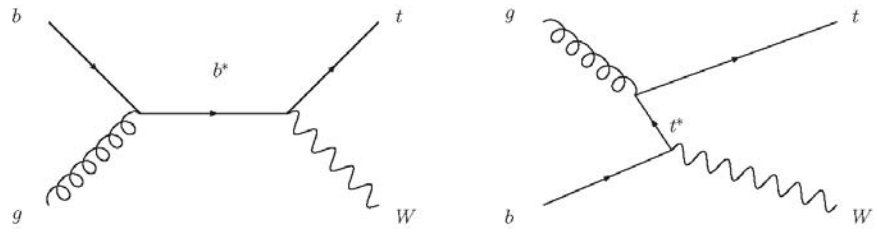

Figure 45: Flavor excitation processes contributing to the dilepton event selection.

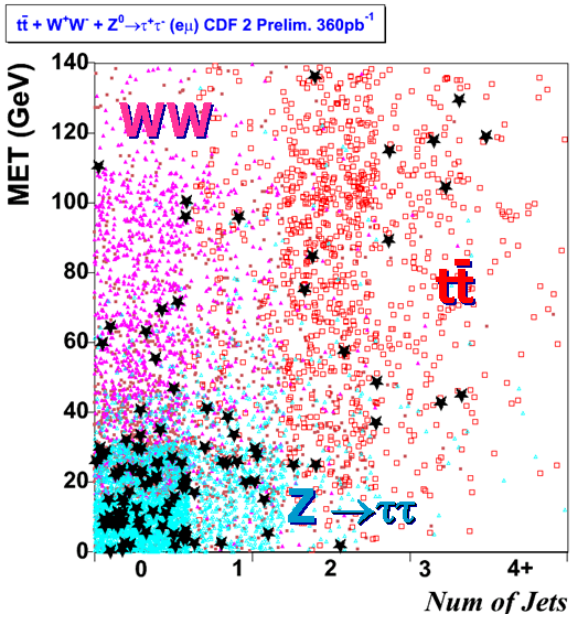

Figure 46: The 2D distributions of jet multiplicities and transverse missing energy for $t\bar{t}$, WW and $Z \to \tau\tau$ compared to Tevatron data.

Without direct mass reconstruction, as here only the transverse mass is available, a successful search in the dilepton channel requires an accurate normalization of standard model contributions to the dilepton event selection and well-described signal kinematics. The transverse mass distribution for $H \to WW$ at $m_H = 160$ GeV is shown in Figure 47. The effect from higher-order corrections on signal kinematics, the Higgs p_T distribution, is shown in Figure 48 and is a source of uncertainty on the dilepton distributions.

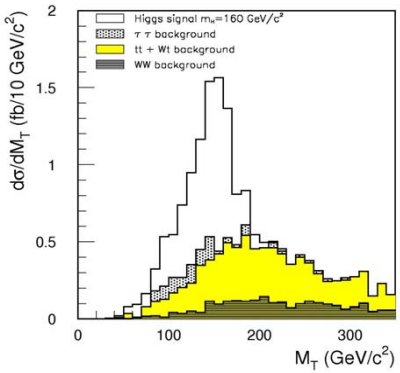

Figure 47: Transverse mass distribution in the $H \to WW \to e\mu\nu\nu$ channel with forward-tagging jet requirements.

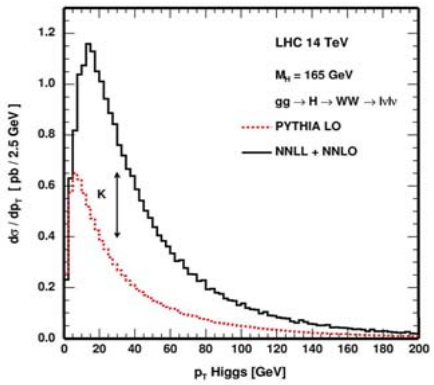

Figure 48: Leading-order event simulations are reweighted for higher-order corrections to the event kinematics.

In the sub-threshold region of the $H \to WW^*$ decay, the requirement of forward-jet tagging, according to the kinematics of qqH production, results in a factor of 10 reduction in background, thereby opening up the low mass search in this channel. Similarly, if the second lepton p_T is too low, then the forward-jets must be included in the trigger decision in order to reduce events from $W + jets$ and multijet QCD background as these would dominate in a single lepton trigger. Forward jets have a transverse momentum of roughly half the W mass, as expected from massive W propagators in the fusion process. The tagging jets occur in the pseudo-rapidities $1.5 < |\eta| < 4.5$ as shown in Figure 40 with corresponding energies of ~ 300 GeV or higher. Figure 49 shows an η-ϕ map of a qqH event with identified forward jets. There is a slow narrowing of jets with energy according to the Q^2 of the jet production, that goes approximately as $E^{-1/4}$. Therefore, tagging jets have a narrower flux of energetic particles than backgrounds consisting of boosted low Q^2 jets, minbias pile-up and reminants from the underlying event.

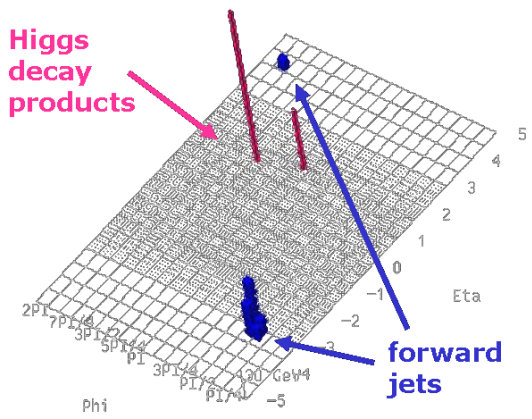

Figure 49: An η-ϕ map of a qqH event with identified forward jets.

The qqH channel with $H \rightarrow WW^*$ loses sensitivity when the effective W^* mass goes below $\sim M_W/2$ resulting in softer second lepton $p_{\rm T}$ spectra. To continue the $H \rightarrow WW^*$ search down to lower masses, the WH production channel can be used. In this channel, there are two nearly on-shell W bosons in the $WH \rightarrow WWW^*$ process. The hard dilepton p_T spectra in this channel increase trigger efficiencies and open up the possibility of a same-sign dilepton search for half of the sample. This signature has very low physics backgrounds especially for dissimilar lepton flavors in the $e^{\pm}\mu^{\pm}$ channel. The soft third lepton may be above reconstruction thresholds, especially for muons, and therefore introduce the trilepton signature. The trilepton and same-sign dilepton searches are high purity analyses and have mainly diboson and instrumental backgrounds. The rejection of the Z peak in the WWW^* signature is effective in removing diboson backgrounds, as shown in Figure 50. The ZH production mechanism would be another source of enhanced triple boson production. The performance of the WWW^* same-sign dilepton search has been studied at the Tevatron for the low mass Higgs search and has a stringent cross section exclusion. The current status of the Tevatron Higgs search is shown in Figure 51.

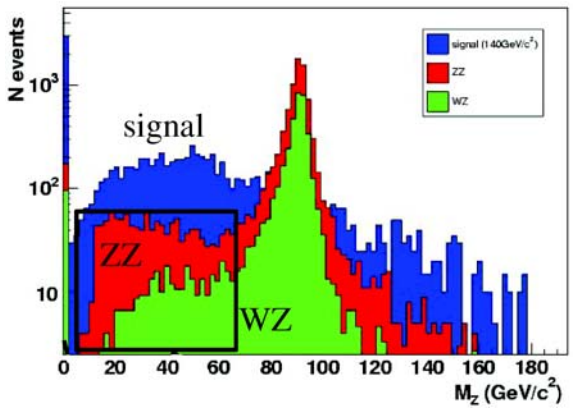

Figure 50: Presence of a Z peak in dilepton combinations from ZZ and WZ backgrounds are rejected in the trilepton $WH \rightarrow WWW^*$ channel. The ZZ backgrounds with $Z \rightarrow \tau\tau$ fall into the signal region as indicated by the boxed region.

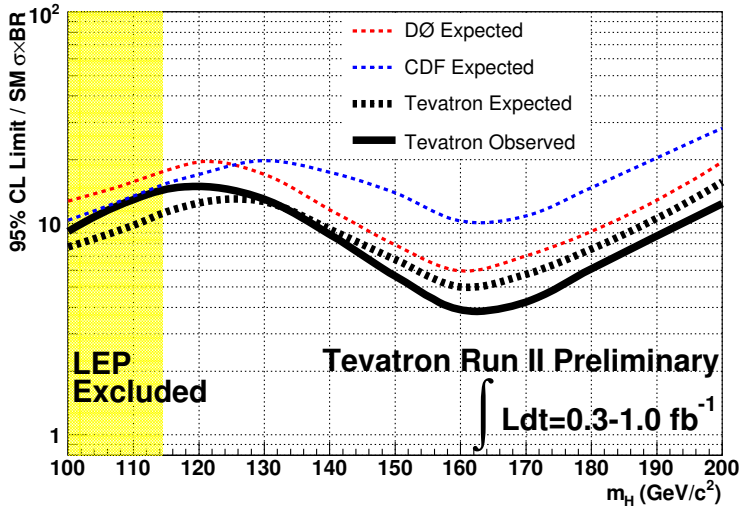

Figure 51: Overall summary of Standard Model Tevatron Higgs searches. The vertical axis is the ratio of the observed limit on the cross section times branching fraction to the expected Standard Model prediction for the Higgs boson.

0.2.4. Boosted Dibosons from Heavy Higgs Decay

As shown in Figure 14, the natural width of the Higgs boson exceeds 100 GeV for a mass of $m_H = 600$ GeV and above, and the total production rate drops to below 1 pb with a significant fraction of the total rate coming from qqH production. To cover this heavy mass region, additional decay channels of $H \to WW$ and ZZ need to be utilized. The highly boosted W and Z bosons coming from an 800 GeV Higgs boson decay will have collimated decay products, as drawn in Figure 52 for the strong WW scattering process. The hadronic decays appear as single jets in the detector. The mass of the single jet can be used to identify the jet as originating from a W or Z boson, as shown in Figure 53. The qqH production mode with $H \to WW \to \ell\nu jj$ and $H \to ZZ \to \ell\ell jj$ decay modes benefit from the higher branching ratios of the hadronic boson decay, and the identification of a massive single jet is an effective part of the event signature. A similar high branching ratio decay channel is the $H \to ZZ \to \ell\ell\nu\nu$ in qqH production. This provides a large transverse missing energy signature as shown in Figure 54.

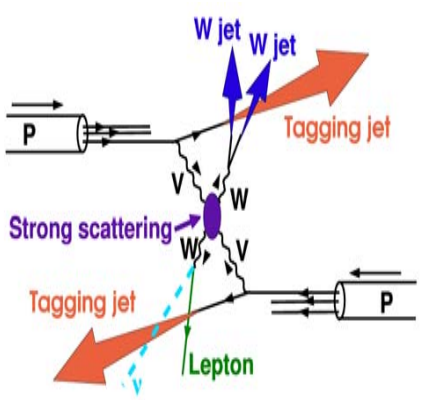

Figure 52: Heavy Higgs production and strong WW scattering event signature.

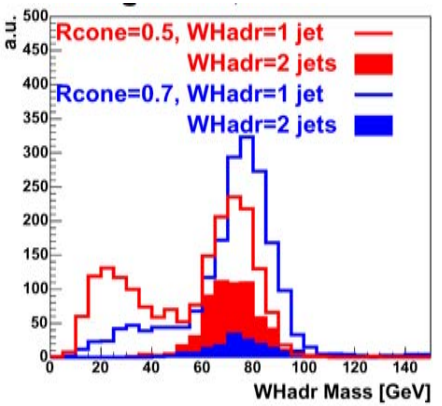

Figure 53: Single-jet W mass reconstruction.

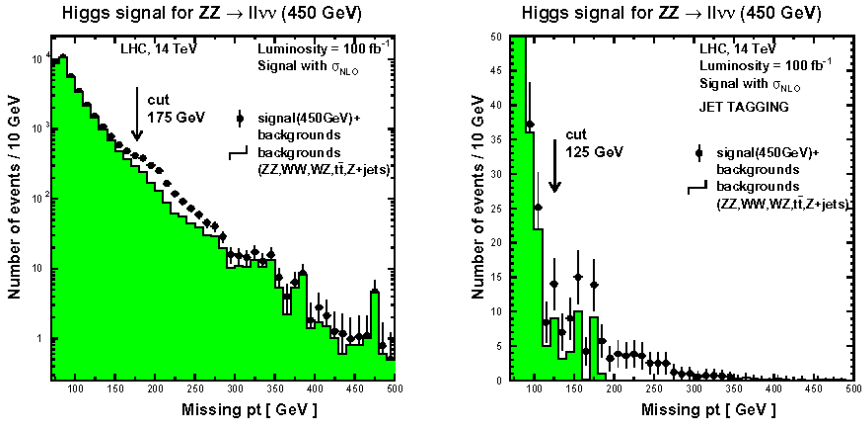

Figure 54: Transverse missing energy distribution in $H \to ZZ \to \ell\ell\nu\nu$ channel without (left) and with (right) requiring forward-tagging jets from weak boson fusion production.

0.2.5. From 115 GeV/c^2 to 1 TeV/c^2

An overview of the Standard Model Higgs search sensitivity with the CMS experiment is shown in Figure 55.

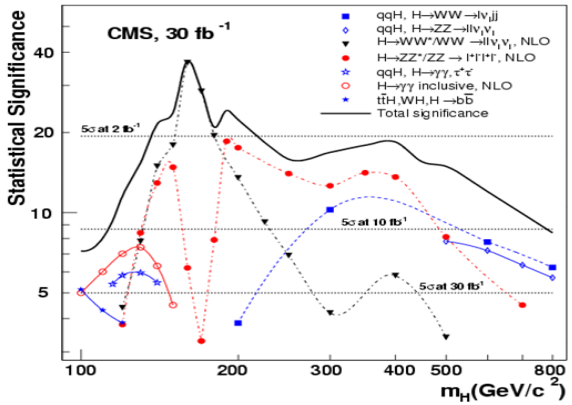

Figure 55: Estimates of the statistical significance of the Standard Model Higgs boson searches with 30 fb^{-1} of integrated luminosity.

The LHC Higgs search has a broader variety of possible analyses than those developed at LEP. Furthermore, the experimental challenges are starkly different in the different search topologies and mass ranges. The high mass resolution channels depend strongly on the calibration and alignment of the tracking, calorimeters and muon spectrometers and are subject to intense commissioning efforts. The JetMET-related search channels must contend with the low p_T jet reconstruction efficiencies and fake rates. The usage of the transverse missing energy in these channels is also subject to commissioning and the effects of detector noise, jet mismeasurement response tails and minbias pile-up. For weak boson fusion search topologies, the forward-tagging jets will be nearly the highest pseudo-rapidity jets used for analysis in hadronic collisions, creating an uncertainty in the reliability of simulations of the jet backgrounds in the forward regions. In cases where the search channel depends on efficient τ-lepton triggering or on single lepton triggers plus jets, techniques for data-driven background calculations must be applied to correctly account for multi-jet QCD backgrounds and instrumental backgrounds enhanced by the trigger selection. Inclusive analyses, such as the dilepton analysis, will have to address a wide variety of standard model processes, some never measured before. The same-sign dilepton and trilepton searches will address rare backgrounds processes with unknown contributions from fake and misreconstructed leptons, requiring data-derived

estimates. Heavy Higgs searches will require dedicated treatment of highly boosted W and Z boson decays. In general, the understanding of the searches starts at high p_T and moves towards lower masses. It would not be surprising in the LHC Standard Model Higgs search to see a rapid exclusion for Higgs boson masses above $m_H \approx 150$ GeV and extending up to 500 GeV, and then followed by more detailed experimental efforts as discussed here to cover the low mass region down to $m_H = 115$ GeV and the high mass region up to 1 TeV.

The LHC Higgs search is a rich landscape and a culmination of nearly all high p_{T} Standard Model physics. MultiTeV-scale physics may have many suprises in store, and the Higgs search may need to dramatically adapt in the next energy frontier. Possible examples of beyond the standard model Higgs searches are discussed in the following section.